Comparing Competing Models of Interaction Cross Sections in ^{27}Al using ^{137}Cs, ^{22}Na, and ^{133}Ba Isotopes

Perrin W. Davidson*
UChicago Department of Physics
(Dated: October 19, 2021)

We conduct a high energy particle counting experiment to determine the limits of the Thomson model in describing the interaction between emitted gammas from ^{137}Cs, ^{22}Na, and ^{133}Ba and the electrons of ^{27}Al. Specifically, we determine the total interaction cross section (including the properly propagated uncertainty) at 7 energy levels. We compare our measured values to the predictions of the Thomson model to assess how well this model represents the results of our experiment. We determine that the Thomson model on average over-estimates the total interaction cross section compared to propagated uncertainties. We attribute these differences primarily to the low energy limit assumed in the model.

I. INTRODUCTION

Counting experiments are a common procedure in physics that help scientists to better understand the unseeable interactions of the world around us. In this experiment, we use a Photomultiplier Tube and Thallium-doped Sodium Iodine (PMT+NaI(Tl)) scintillator to make measurements of the energy and counts of gammas (high energy photons) emitted from Cesium-127 (^{137}Cs), Sodium-22 (^{22}Na), and Barium-133 (^{133}Ba) in an energy range from ∼30keV to ∼1.2 MeV as they pass through Aluminum-27 (^{27}Al). We use these measurements to calculate the total interaction cross section, σ_{cs}, and determine the accuracy of the classical Thomson scattering model in predicting σ_{cs}. We also use these measurements to identify the dominant adsorption mechanisms of the interaction between emitted gammas in this experiment and ^{27}Al.

I.1. Thomson Scattering

To derive the classical equation for Thomson Scattering we will use in this experiment, we start with the electromagnetic equation of a wave [1]:

$$\boldsymbol{E} = E_0 \exp\left[i(\boldsymbol{k}\cdot\boldsymbol{r} - \omega t\right]\boldsymbol{e}, \tag{1}$$

where E_0 is the amplitude of the electric field, $\boldsymbol{k}$ is the wave vector, $\boldsymbol{r}$ the position vector, ω the angular frequency, t the time, and $\boldsymbol{e}$ is the polarization vector. We know that the equation of motion for a charged particle of charge q and mass m corresponding to this description is given by:

$$\boldsymbol{F} = q\boldsymbol{E} = m\ddot{\boldsymbol{s}}. \tag{2}$$

We know from electricity and magnetism that the power radiation by an accelerating, non-relativistic charged particle is:

$$\frac{\mathrm{d}P}{\mathrm{d}\Omega} = \frac{q^2\langle\ddot{\boldsymbol{s}}\rangle}{16\pi^2\epsilon_0 c^3}\sin^2\theta, \tag{3}$$

where we also know that:

$$\langle\ddot{\boldsymbol{s}}\rangle = \frac{q^2}{m^2}\langle\boldsymbol{E}^2\rangle = \frac{q^2E_0^2}{2m^2}. \tag{4}$$

Furthermore, we can calculate the time-averaged Poynting flux of the incident wave as:

$$\langle u\rangle = \frac{\epsilon_0 c E_0^2}{2}. \tag{5}$$

Then, defining the differential interaction scattering cross section as

$$\frac{\mathrm{d}\sigma_{cs}}{\mathrm{d}\Omega} = \frac{\mathrm{d}P}{\mathrm{d}\Omega}\frac{1}{\langle u\rangle}.$$

Combing these equations gives:

$$\sigma_{cs} = \int_0^\pi \frac{\mathrm{d}\sigma_{cs}}{\mathrm{d}\Omega}2\pi\sin\theta\,\mathrm{d}\theta \tag{6}$$

$$= \frac{8\pi}{3}\left(\frac{q^2}{4\pi\epsilon_0 mc^2}\right)^2. \tag{7}$$

Eq. (7) is the equation we employ in calculating the Thomson scattering total cross section in this experiment for the mass and charge of an electron. Note that this equation is independent of incident photon energy and treats the electron as a solid sphere that is one body within an elastic scattering of the incident electromagnetic radiation.

Additionally, it is important to note that this is the low-energy limit of Compton Scattering, meaning that the electron's kinetic energy and incident photon frequency do not change throughout the interaction [2]. This equation is valid within in the limit of the photon energy being much smaller than the mass energy of the electron. Our experiment will test whether or not this limit is indeed valid for the 7 energies of gammas we tested.

I.2. Linear Attenuation Composition

In general, we define the linear attenuation as the sum of three process [3]:

$$\lambda = \tau_{pe} + \sigma_C + \kappa. \tag{8}$$

* pwd@uchicago.edu

These three processes that we consider that dominate the interaction of the incident photon with the electron are Compton Scattering (σ_C), the Photœlectric Effect (τ_{pe}), and Pair Production (κ). Compton Scattering describes a photon electromagnetically colliding with an electron, in so doing transferring an amount of energy to the electron, unlike the classical Thomson Scattering description. Compton Scattering is possible at all energies. The Photœlectric Effect is when a photon is fully absorbed by an atom, which liberates an electron from the atom's shell in the process but is only possible at low energies. Finally, Pair Production is when a photon is split into an electron-position pair when the photon has more energy than twice the mass of the electron, or $E \geq 2m_e c^2$.

I.3. Experimental Cross Section

In this experiment, we define the rate of intensity of a beam of incident photons as [4]:

$$\mathrm{d}R = -N_d \sigma_{cs} R \, \mathrm{d}x \,, \tag{9}$$

where R is the intensity, N_d is the electron density, and $\mathrm{d}x$ is the thickness of a material (which we will also call an absorber) through which the photon are passing. We can calculate the electron density using:

$$N_d = \frac{\rho Z}{A}, \tag{10}$$

where ρ is the mass density of the material, Z is the atomic number, and A is the atomic mass. Solving Eq. (9) leads to our equation for intensity:

$$R(x) = R_0 e^{-\lambda x} + B, \tag{11}$$

where we define the linear attenuation cœfficient as

$$\lambda = N_d \sigma_{cs}. \tag{12}$$

Note the term B. This is a constant background value added to the fit. Given the form of the exponential which drives the rest of the equation, this background constant allows the fit to essentially be raised or lowered depending on the data and thus get a better fit as determined through "goodness of fit" measurements.

II. METHODS AND MATERIALS

II.1. Experimental Set-Up

We use a Photomultiplier Tube (PMT) and Thallium-doped Sodium Iodide (NaI(Tl)) scintillator to indirectly "count" the photons that pass through the absorber via measured voltage pulses [4]. With each interaction of the gammas with the absorber, some amount of energy is given to the absorber. The PMT-NaI(Tl) is our way of "measuring" this amount of energy and estimating the number of gammas passing into the detector. Iodine is dense with electrons, so there is a large interaction cross section for the gammas to interact and excite the Tl, which in turn emit photons when the dopant de-excites. This process is known as scintillation and the resultant light is measured in the PMT.

Comprised of numerous plates called dynodes, the scintillation photons emitted by the Tl NaI(Tl) strike the first dynode of the PMT, which in the process releases electrons via the photœlectron effect which then race toward the second dynode, at a slightly higher potential. This process continues down the PMT, consecutively producing more and more electrons than the number of incident electrons. A multiplication factor is determined from the output voltage. This output voltage is proportional to the amount of energy deposited in the NaI(Tl) crystal by the incoming photon. It is these oncoming pulses that we use to measure the energies of the gammas.

In practice, the PMT-NaI(Tl) was connected to a Pulse Height Analyzer (PHA) via a 50 Ω terminator. The PHA was then connected to USX software and the data collected on a local machine. Importatly, the high voltage setting was used and set to +1000 for all measurements.

We then use this PMT-NaI(Tl) to count the number of photons that pass through a range of absorber thicknesses, in-so-doing allowing us to apply the Eq. (11) to estimate the linear attenuation cœfficient. Therefore, the set-up was: radioactive source, absorber, then PMT-NaI(Tl) from bottom to top of a metal armature. The distance between the source and the PMT-NaI(Tl) was approximately 30 cm. The distance between the source and the absorber was approximately 10 cm.

Isotope	Decay Energies (keV)
^{137}Cs	32, 662
^{22}Na	511, 1275
^{133}Ba	31, 81, 356

TABLE I. Decay energies for the three radionuclides used to emit gamma radiation, specifically ^{137}Cs, ^{22}Na, and ^{133}Ba. The counts of gammas at each of these energies are what were used to determine the intensity, R.

II.2. Materials

In this experiment, we used the radioactive isotopes ^{137}Cs, ^{22}Na, and ^{133}Ba to emit our gammas that pass through our absorber, ^{27}Al. The energies of these gammas were subsequently measured by the PMT-NaI(Tl). The decay energies for each of these radionuclides are presented in Table (I). These were determined by looking at each radionuclide's decay scheme.

II.3. Experimental Procedure

For each of the three sources, we first took a spectrum of the background radiation for error calculations, in which there were no sources or absorbers present. We then measured the source without any absorber before measuring 5 to 6 separate spectra with varying absorber thicknesses, ranging from approximately 0.1 cm to 10 cm. At each spectrum measurement run, we measured each absorber thickness, recording everything in our lab notebook. The high voltage and gain setting per source were also collected.

For every source, a different set of Regions of Interests (ROIs) were chosen based on the energies emitted by each source presented in Table I, which we attained by reviewing each radionuclides' decay scheme. These regions were used as the bounds of summation of all counts within the peak range corresponding to each energy. Within each ROI, we measured and recorded the gross and net counts, where the net counts were calculated after subtracting the linear trend over the ROI. These peaks were chosen after calibrating the channel to be proportional to each energy of interest, which was done within the USX software using a 2-point calibration scheme. We subscribed to selecting the region bounds as being at least below the full-width half-maximum of each peak. The time of each run per energy was constant and set within the USX software but varied based on the source to allow for the fractional uncertainty of each count measurement to be only a few percent. Our uncertainty values ranged from $< 1\%$ to $\sim 3\%$.

Each measurement was quickly plotted and examined in Excel and Python to ensure that the measurement data was acceptable (i.e., the fractional uncertainty was within reason) and no more measurements were needed to be taken.

II.4. Uncertainties

To calculate the net number of counts per energy that were used in our calculations, we subtracted the background (B) for each source from the gross (G) counts per energy [4]:

$$N = G - B. \tag{13}$$

We estimated the uncertainty in these calculations following the Poisson distribution:

$$\delta N = \sqrt{\delta G + \delta B}, \tag{14}$$

where the individual uncertainties are $\delta G = \sqrt{G}$ and $\delta B = \sqrt{B}$.

III. RESULTS

III.1. Observed Spectrum

A spectrum of the observed ^{137}Cs data with no absorber present during measurement is shown in Fig. (2). There

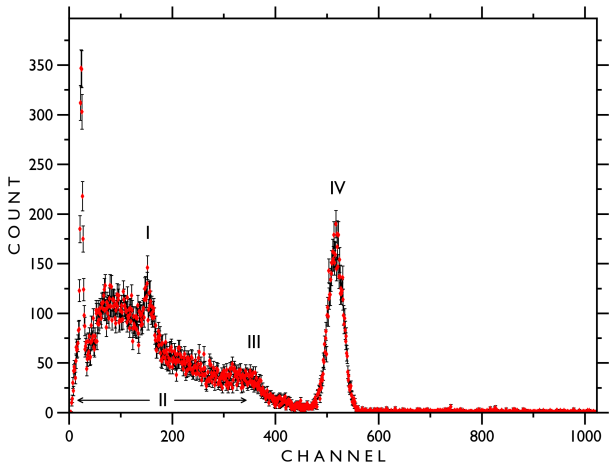

FIG. 1. Annotated spectrum from ^{137}Cs data with no absorber present during measurement. (I) is the Backscatter Peak, (II) is the Compton Shelf, (III) is the Compton Edge, and (IV) is the Full Energy Peak. The red diamonds are the measured counts per channel and the black intervals are the Poisson errors defined by Eq. (14).

are four important features, identified (I) through (IV), in this plot. The first (I) is the Backscatter Peak (E_{BS}). This occurs when some photons that are initially traveling away from the detector scatter back into the detector. This can occur at many different angles and energies. However, as we have vertically aligned our source and PMT-NaI(Tl) detector, a 180 degree backscatter is most likely to have caused this peak, essentially when the photon scatters off of the counter top.

The second element (II) of this spectrum is the Compton Shelf, or Compton Plateau. This occurs when a photon Compton Scatters before escaping the detector and therefore only deposits some of its energy into the detector. There is a range of energies that this can happen at, however the maximum energy transfer occurs when a photon scatters at 180 degrees within the detector. This leads to the third element (III) of the spectrum, the Compton Edge (E_{CE}). The final element (IV) is the Full Energy Peak (E_γ) occurs when a photon deposits all of its energy into the detector. The result is a Gaussian-like peak at a centroid that is proportional to the decay energy from the source. We can relate these elements by:

$$E_\gamma = E_{CE} + E_{BS}. \tag{15}$$

III.2. Fitted Spectrum

We fit the gamma spectrum described in Sec. III.1 using a Gaussian model with a linear trend given by:

$$f(x) = \frac{N}{\sigma\sqrt{2\pi}} e^{-(x-\mu)^2/(2\sigma^2)} + Ax + B, \tag{16}$$

where N is the number of net counts in the peak, σ is the standard deviation, μ is the centroid, and A and B are the

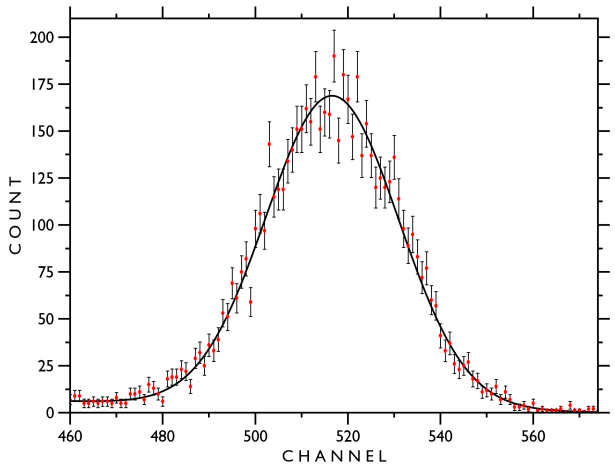

FIG. 2. Fitted spectrum from ^{137}Cs data with no absorber using the Levenberg-Marquadt algorithm for least-squares. The fitted function was a Gaussian model with a linear background trend given by Eq. (16). The red diamonds are the measured counts per channel and the black intervals are the Poisson errors defined by Eq. (14).

cœfficients of the terms in the linear background.

The fitted parameters with calculated uncertainties are presented in Table II. The uncertainties for the least-squares parameters N, μ, σ, A and B were calculated from the Levenberg-Marquadt algorithm implementation of the generalized non-linear least squares method. This method works to minimize the squared sum of the fit residuals normalized by the uncertainty, ϵ:

$$\chi^2 = \sum_{i=1}^{N-1} \left(\frac{\widehat{y}_i - y_i}{\epsilon_i} \right)^2, \tag{17}$$

where $\widehat{y}_i$ is the fit value and y_i the measured value. The uncertainty in each estimated parameter is determined by the variance in the parameter estimate, given generically for a parameter function $\Theta(\boldsymbol{x})$ by [5]:

$$\sigma_\Theta^2 = \sum_{t=0}^{N-1} \sigma_i^2 \left(\frac{\partial \Theta}{\partial x_i} \right)^2 \tag{18}$$

where $x_i \in \boldsymbol{x}$ are the parameters being fit and σ_i^2 the variance in each parameter fit. The χ^2 goodness of fit statistic was calculated following :

$$\chi^2 = \sum_{i=1}^{N} \left(\frac{\widehat{y}_i - y_i}{\epsilon_i} \right)^2, \tag{19}$$

similar in construction to Eq. (17). The Degrees of Freedom were calculated following:

$$N_\nu = \text{length}(y) - \text{length}(x) \tag{20}$$

where y are the number of data points being fitted and x are the parameters being fitted.

Parameter	Fitted Value
N	5949.67 ± 85.54 (counts · channel)
μ	516.64 ± 0.21 (channel)
σ	14.33 ± 0.18 (channel)
A	-0.05 ± 0.01 (counts/channel)
B	30.34 ± 3.72 (counts)
χ^2	109.7
N_ν	110
χ^2_ν	1.00

TABLE II. Fitted parameters of ^{137}Cs spectrum with no absorber. All units are presented when physically consistent. N is the number of counts in the spectrum, μ is the mean of the Gaussian, σ is the standard deviation, A is the slope of the linear background term, B is the dependent axis intercept, χ^2 is the chi-squared statistics, N_ν are the degrees of freedom, and χ^2_ν is the reduced chi-squared statistic.

III.3. Linear Attenuation

We fit the count rate R as a function of absorber thickness, x, using Eq. (11). These observational data were fit using the Levenberg-Marquadt algorithm implementation of the generalized non-linear least squares method and the errors associated with these values are calculated from this implementation.

The count rate was calculated following:

$$R = \frac{N}{t}, \tag{21}$$

where N is the net number of counts calculated from Eq. (13) and t the time elapsed in measuring those counts. Then, the uncertainty in this calculation was estimated following:

$$\delta R = \sqrt{\left(\frac{\delta N}{N} \right)^2 + \left(\frac{\delta t}{t} \right)^2}, \tag{22}$$

where δN was calculated using Eq. (14) and δt was the precision of the PHA/USX system, which was 1 second for the entire experiment. Fig. 3 presents the 7 different energies and associated rates per absorber thickness by source.

From the fitting, we were able to obtain a least-squared estimate of the linear attenuation cœfficient, λ, with error bounds as calculated by the Levenberg-Marquadt algorithm and described previously. We present these linear attenuation cœfficients for aluminium and errors in Table III. Additionally, we compare these values to those from the NIST. To properly compare these values, we interpolated using a cubic smoothing spline to our energies. The errors on each NIST value were assumed to be 3%. After calculating the error per NIST point, these errors were then also interpolated using the same cubic smoothing spline method.

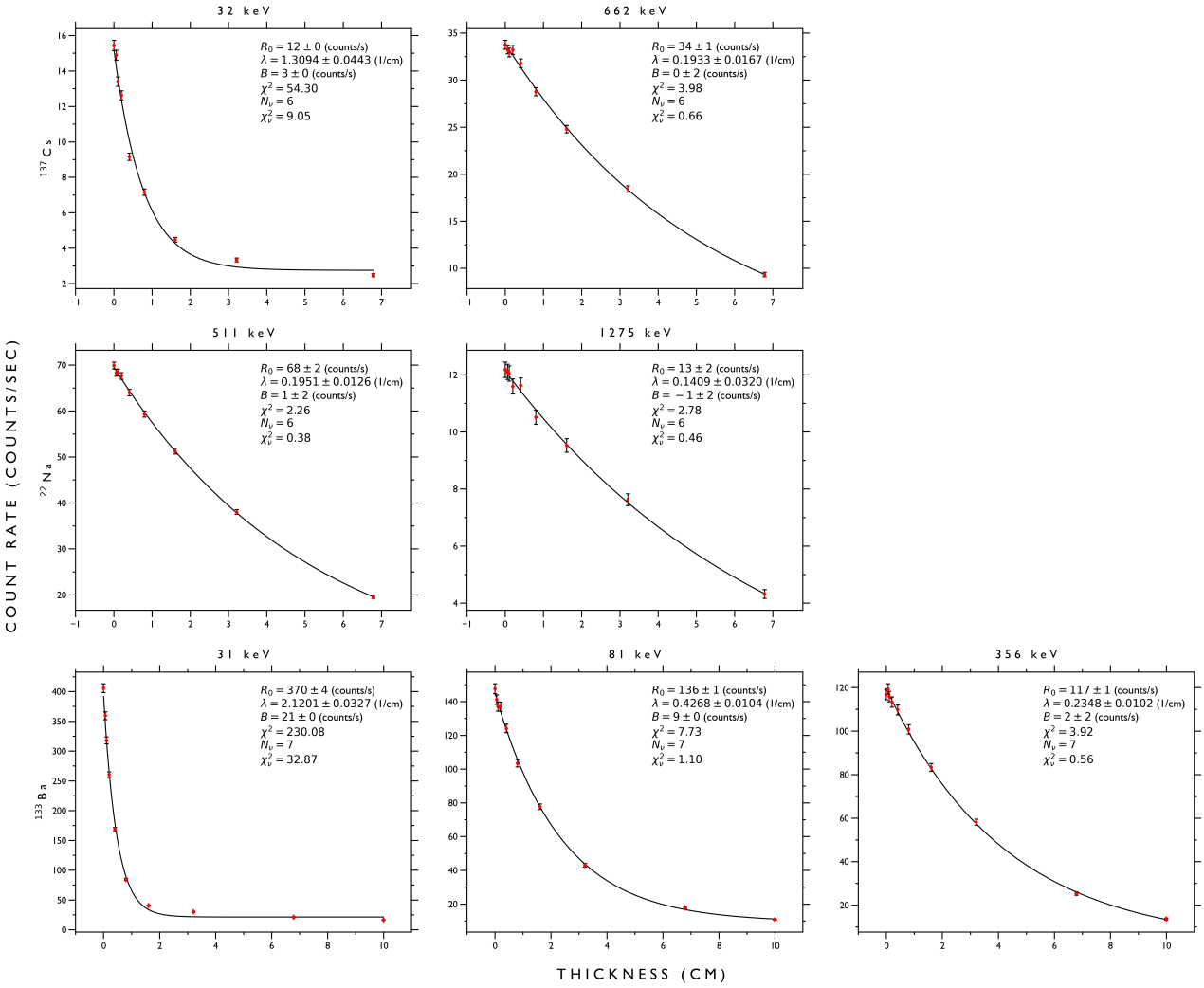

FIG. 3. Fitted rate of intensity, R, over absorber thickness, x, plots for 7 different energies (labeled at the top of each plot) across three sources, ^{137}Cs, ^{22}Na, and ^{133}Ba (labeled per row). The red diamonds are the observed points and the black bars the errors per point, calculated following Eq. (22). The fit is presented in the solid black line. Additionally, the calculated fit parameters are presented, as well as the goodness of fit parameters. R_0 is the amplitude of the exponential, λ is the linear attenuation cœfficient, B is the constant background parameter, χ^2 is the chi-squared statistics, N_ν is the degrees of freedom, and $\chi^2_\nu = \chi^2/N_\nu$ is the reduced chi-squared statistic. Considering that $\chi^2_\nu \leq 1$ is considered a "good fit", it is interesting to compare this against the finding form the p-value test.

III.4. Cross Sections

Also presented in Table III are the cross sections for every energy measured. This was calculated by first finding the density of aluminum using Eq. (10). Taking $\rho = 2700$ kg/m^3, $Z = 13$, $A = 0.02698$ kg/mol and Avogadro's number to be 6.022×10^{23} atom/mol, we get that $N_d = 7.834 \times 10^{29}$ m^{-3} [6]. Then, we can use Eq. (12) to calculate those presented in Table III. Importantly, we multiply those values presented in Table III by a conversion factor of 100, to ensure that we are dealing in units of meters.

We compared these values to those predicted by Thomson scattering, which is the low energy limit of Compton scattering. Using Eq. (7) for an electron, with $m = 9.1093837015 \pm 0.0000000028 \times 10^{-31}$ and $q = 1.602176634 \pm 0.000000000 \times 10^{-19}$, we find that Thomson Scattering predicts a total interacting scattering cross section is $6.65 \times 10^{-29} \pm 4.09 \times 10^{-38}$m^2 [7, 8]. To calculate the error associated with the Thomson model, we use the following calculation:

$$\delta\sigma_{TM} = 2\sigma_{TM}\frac{\delta m_e}{m_e}, \tag{23}$$

where m_e is the mass of the electron and δm_e its uncertainty.

The average of our calculate cross section values is $8.42 \pm 0.29 \times 10^{-29}$m^2. While this is not strictly within uncertainty of the Thomson model, we are certainly within the the same

Energies (keV)	λ (cm^{-1})	λ_{NIST} (cm^{-1})	σ_{sc} (10^{-28} m^2)
31	2.12 ± 0.03	2.79 ± 0.09	2.71 ± 0.04
32	1.31 ± 0.04	2.58 ± 0.07	1.67 ± 0.06
81	0.427 ± 0.010	0.542 ± 0.015	0.545 ± 0.013
356	0.235 ± 0.010	0.261 ± 0.013	0.300 ± 0.013
511	0.195 ± 0.013	0.220 ± 0.012	0.249 ± 0.016
662	0.193 ± 0.017	0.204 ± 0.011	0.247 ± 0.021
1275	0.141 ± 0.032	0.154 ± 0.008	0.180 ± 0.041

TABLE III. Calculated ^{27}Al linear attenuation cœfficients from 7 different energies and 3 sources. λ are the values calculated from this experiment, λ_{NIST} are the values calculated from the NIST standards, and σ_{cs} are the calculated total interacting cross section per energy.

Energies (keV)	P-Value	χ^2_ν
31	4.7×10^{-46}	33
32	6.4×10^{-10}	9.1
81	0.36	1.1
356	0.79	0.56
511	0.89	0.38
662	0.68	0.66
1275	0.84	0.46

TABLE IV. Calculated p-values and reduced χ^2 statistics for every energy value fit across three radioactive sources. The importance of these estimates is to determine the "goodness of fit" of each fitted negative exponential function. A typical significance value is taken as $\alpha = 0.95$. Therefore, the values presented here are, on average, not significant and indicate not "good fits." Note the inverse relationship between the p-value and the reduced χ^2, χ^2_ν.

order of magnitude and spread of our data. To see that our data clearly surrounds and passes through the Thomson model prediction, see Fig. 4.

IV. DISCUSSION

IV.1. Measurement Uncertainties

One of the sources of uncertainty in the gamma counting routine is the assumption that we are following a Poisson distribution and that the error is truly equal to the square of the number of counts. However, as we are fitting with Gaussians (both the fitting function but also the underlying assumption of non-linear least squares), we can say that we are living in a Gaussian world and these assumptions are justified. This is over simplistic and contributes some error.

Additionally, the assumption that the background is linear as seen in Eq. (14) is another source of error. While this is better than the automated calculation of error that was done by the USX software, we still do not know the full extent of the background at the moment that we measured the sources, as our background was constantly changing – from the time-dependent actions of other students transporting radionuclides to the decay of other materials in the lab.

However, if we assume these events are random and normally distributed – as is often done in many of the techniques we used in this, such as smoothing splines and least squares methods – then our sample was, most likely, representative of this assumption and valid. Despite this, it is important to understand these possible biases when analyzing our data.

IV.2. Fitted Spectrum Uncertainties

The goodness of fit parameters can be interpreted as follows. The chi-squared tests to see if the fit that we outputted was expected. It is the sum of the square of the error normalized residuals between the fit and the observed value. This is to say that this test tells us, given the error in our estimate at a given point, how far the fit is from the observed value. If we take every observed value to be a decomposition of a "true value" and a "noisy" value — of the form $y_i = \widehat{y}_i + \epsilon_i$ — then the chi-squared statistics essentially tells us how well the fit did in balancing the error against the observed value. The reduced chi-squared statistic — which is the chi-squared test normalized over the degrees of freedom — then tells us for every point, how well the fit is performed. We can think of this as an average "goodness" of the fit over the dataset, per data point.

It is important to analyze the "goodness of fit" metrics χ^2 and $\chi^2_\nu = \chi^2/N_\nu$ for our Gaussian fit to the ^{137}Cs spectrum. The χ^2 test is a statistical measurement of the probability that the fit would be realized. To determine this probability from the χ^2-distribution and degrees of freedom, we use the function `pchisq` in R. For $N_\nu = 110$ and $\chi^2 = 109.7$, the associated p-value is 0.490. For a "good fit" we would want a significantly higher value (probability), such as the canonical significance value of $\alpha = 0.95$. Therefore, we can conclude that this fit is "not good".

Another measure of the goodness of the fit to this spectrum is the reduced χ^2 statistic, χ^2_ν. The standard rule is that a statistics of $\chi^2_\nu = 1$ is a fit such that the balance between the observations and estimates is in accord with the error variance, essentially that it is neither over- or under-fitting the data. More generally, we say that $\chi^2_\nu \leq 1$ is a "good fit". However, you can run into problems of over-fitting — where the model is improperly fitting noise or the error variance is overestimated — for $\chi^2_\nu \ll 1$.

IV.3. Fitted Linear Attenuation Cœfficient Uncertainties

Looking at the p-value for each of the 7 energies presented in Table IV, we can see a spread of goodness of fit for the fitting of the linear attenuation cœfficients. Specifically, the inverse relationship between the p-value and the χ^2_ν can clearly be seen, with the lower energies having poorly fit data whereas the higher energies have better fits. Specifically, the p-values for energies 356 to 1275 represent a high probability of those fits occurring, backed up by the χ^2_ν val-

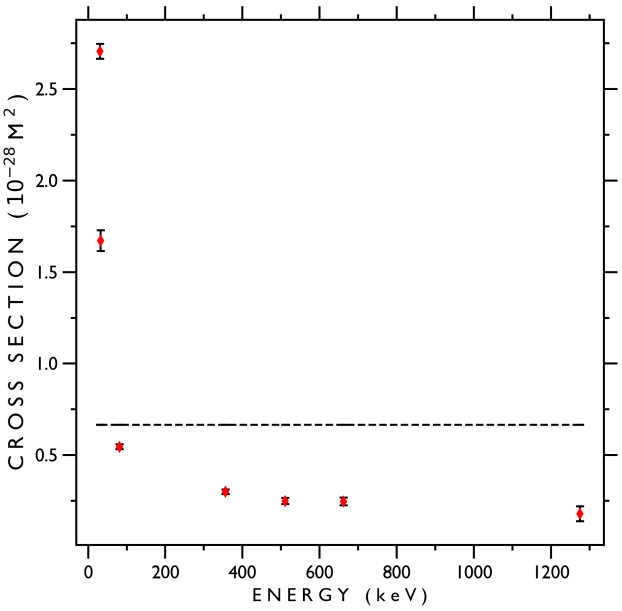

FIG. 4. Calculated cross sections from 7 energies across 3 different radioactive sources plotted against the Thomson model. The red diamonds are the calculated cross section with associated errors in black bars, calculated from Eqs. (7) and (23). The dash black line is the Thomson model.

ues less than 1. We do run the risk of over-fitting these data given these statistics, but at least we are within the "good fit" range.

There are no anomalies in the data presented in Fig. 3. However, it is important to note that the exponential fit was not perfectly achieved in the data for every source. The sodium and cesium data points were measured on one day. As can be seen, at the higher energies, that exponential curve that we are fitting was not really reached as we did not have thick enough absorbers. Learning from these mistakes, the barium spectra have a much more classic negative exponential form as we took thicker measurements on the second day. Therefore, we can be more confident in our fit here, as the data and fit takes into consideration the form of the negative exponential best here. It is really those tail-end points as the exponential starts to flatten out that matter most when performing this fit. Therefore, including those is incredibly important.

We can see from the data that for only 2 of our data points agree with the literature values, within error. The remaining 5 data points are outside of error bounds. The mean deviation between our values and the NIST's was 0.303 (cm^{-1}) or about 28% off of the literature values. It is interesting to note that for the energy with the most "canonical" exponential curve, being ^{137}Cs's 32 keV, we had the largest discrepancy, with a 98% discrepancy from the literature values.

Energies (keV)	Dominant Mechanisms
31	Photœlectric Effect
32	Photœlectric Effect
81	Compton Scattering
356	Compton Scattering
511	Compton Scattering
662	Compton Scattering
1275	Compton Scattering

TABLE V. Dominant mechanisms of each gamma energy measured as presented in Eq. (8). The majority of the energies are dominated by Compton Scattering. The crossover from dominance by the Photœlectric Effect to Compton scattering occurs approximately at 50 keV.

IV.4. Cross Section Uncertainties and Comparison

Looking at Fig. 4, we can compare the differing calculated cross sections. First, note the difference between those calculated from our data and that predicted by the Thomson model, specifically the discrepancy at higher energies. This is understandable as we are in a low energy limit for many of these energies, where the Thomson model is applicable, and it is at these lowest energies where our cross section values approach the Thomson model.

Note the lowest energy values are one order of magnitude greater than the Thomson model. This is most likely due to the fact that the energy deposition from the photon to the electron is not taken into account in the Thomson model. However, as we would start to approach the higher energies, we would start to see this model at once approach the Thomson model value and then decrease, as can be seen in Fig. 4. In the data, we can see a general trend steadily decreasing from the predicted cross section from the Thomson model. This is understandable as with the higher energy, there will be a greater deposition of the photon energy into the electron, the contribution of the photœlectric effect is less and Compton Scattering as the dominant mechanism increases.

Looking at the Harshaw Radiation Detector Catalog plot of linear attenuation cœfficients for aluminum, we can understand the dominant mechanics in the absorption. These are presented in Table V. In the energies 31 and 32, the interactions are dominated by the photœlectric effect. However, in the energies 81 to 1275 keV, the major process dominating the interactions is Compton Scattering, with the contribution of the photœlectric effect steadily decreasing nearly linearly on the log scale. This would lead to increasingly worse estimates of the cross section by the Thomson model as the low energy limit is slowly violated. Pair Production dœs not come into play until well beyond the energies that we are dealing with this experiment.

V. CONCLUSION

Through our analysis, we conclude that the Thomson model is best in the low energy limit and over-estimates the interaction cross section for high energies. We suggest that this is due to the classical (non-relativistic) assumptions that go into deriving the model. Next steps would be to compare our experimental data to model output for Compton Scattering, which takes into consideration relativistic effects. As we know from Table V, this model is dominant across most of the spectrum and checking this would help to compare the strengths and weaknesses of the Thomson model.

Additionally, we find that our experimental data and propagated error fall near and within those values presented in the literature for the linear attenuation cœfficients of ^{27}Al. The next step here is to conduct this experiment to determine the linear attenuation cœfficients for different materials. How dœs this change the linear attenuation cœfficients? The interaction cross section? By conducting these experiments, we would be able to better understand how the cross section changes by material.

This experiment therefore shows that high energy particle counting such as the procedure conducted as part of this experiment indeed presents a glimpse into the microscopic interactions we are unable to see in the everyday world.

ACKNOWLEDGMENTS

I would like to acknowledge my lab partner, Tristan Bachmann, for their help on this project.

[1] S. L. Prunty, Physica Scripta **89** (2014).
[2] M. J. Cooper, Reports on Progress in Physics **48**, 415 (1985).
[3] *Photon Cross Sections, Attenuation Cœfficients, and Energy Absorption Cœfficients From 10 keV to 100 GeV*, Tech. Rep. 29 (National Bureau of Standards, U.S. Department of Commerce, 1969).
[4] M. Chantell, D. McCowan, and K. V. D. Bogart, *Introductory Lab — Gamma Cross Sections*, Department of Physics, The University of Chicago (2021).
[5] M. Chantell, D. McCowan, and K. V. D. Bogart, *Linear Least-Squares Fitting*, Department of Physics, The University of Chicago (2021).
[6] J. S. Coursey, D. J. Schwa, J. J. Tsai, and R. A. Dragoset, *Atomic Weights and Isotopic Compositions*, National Institute of Standards and Technology (2015).
[7] *Fundamental Physical Constants: electron mass*, National Institute of Standards and Technology (2018).
[8] *Fundamental Physical Constants: elementary charge*, National Institute of Standards and Technology (2018).